A Pore-Skeleton-based Method for Calculating Permeability and Capillary Pressure

Xinling Li[a], Zeyun Jiang[*,b,c], Jingsheng Ma[b], Tianshen Huang[b], Xin Wang[d]

[a] School of Mathematical Sciences, University of Electronic Science and Technology of China, Chengdu, China
[b] Institute of Petroleum Engineering, Heriot-Watt University, Edinburgh, UK
[c] School of sciences, Southwest Petroleum University, Chengdu, China
[d] Institute of Oceanographic Instrumentation, Shandong Academy of Sciences (SDIOI), Qingdao, China

*Corresponding author (Zeyun.Jiang@hw.ac.uk)

Abstract

We have developed a new method for calculating permeability and capillary pressure from the pore skeleton that is extracted from a fractured rock model, which might comprises medial axes of matrix pores and/or medial surfaces of fracture voids. Such a skeleton, therefore, is able to encapsulate the total connected fluid flow paths in the pore-void space. To do pore network flow simulations, the pore skeleton needs to be further 'discretized' into a network of interconnected nodes and bonds to capture local pore morphology. Jiang et al. (2017) developed a method to extract pore skeletons of this type and a discretization to construct a pore network model that is optimal in many aspects. In this work, we develop a new in-place discretization method, by simply inserting a virtual link, a bond, between every pair of skeleton voxels, nodes, which are either face or only edge adjacent under certain conditions. This new method results in a simpler pore network model, i.e. a virtual network, in which each node or bond is assumed as either a cylinder or a tiny fracture, as well as prescribed with length and inscribed radius/aperture only. As a result, a simpler pore network simulator is also developed using improved formulae of conductance and capillary pressure according to where each virtual link falls, appropriately distinguishing every local configuration within matrixes or fractures. We verify our methods by comparing the simulation results against with those of lattice Boltzmann methods and a laboratory flooding experiment and demonstrate the accuracy and efficiency of our methods with sensitivity analysis.

Key words: Medial axes, medial surfaces; fracture aperture; permeability; capillary pressure

1. Introduction

It is well-known that more than 60% of oil and 40% of gas reserves worldwide are held in carbonate reservoirs. Due to the complex processes of sedimentation and diagenesis carbonate rocks exhibit extremely heterogeneous pore structures with broad pore sizes, for instance, ranging from half-micron to centimeter length scales, with irregular pore shapes and with various pore connectivities that are at and crossing multiple length scales (Arns et al. 2005; Jiang et al. 2013; Andrew et al. 2014). Moreover, carbonate reservoir rocks are widely fractured (Geiger and Emmanuel 2010), where fractures at various length scales commonly penetrate rock matrixes irregularly and may intersect each other. The recovery of hydrocarbons in carbonate reservoirs is very low, therefore the selection of effective production mechanisms relies on a comprehensive characterization of carbonate reservoir rocks in terms of the measured flow properties that are reliable for reservoir-scale modellings.

Special core analysis (SCAL) is a standard experimental approach to measure rock macroscopic properties (Rose and Bruce 1949; Richardson et al. 1952). Despite being expensive, however, SCAL alone does not offer any insights into the processes taking place within the complex of carbonate pore systems that are crucial for interpreting SCAL measurements. Numerical approaches, which are based on 2D or 3D voxel representation (image or model) of porous media, become *de facto* workflows in

the advent of X-ray computed tomography (e.g., Wildenschild,Sheppard 2013; Karpyn et al. 2007) and the maturity of 3D reconstruction algorithms (e.g., Øren and Bakke 2002; Wu et al. 2006; Huang et al. 2017). With 3D rock models, i.e. tomographic images or reconstructed voxel-representations, there are two major numerical approaches to simulate single- and multi-phase flow processes: direct simulation and pore network modelling. The direct simulation method includes finite element/volume methods (e.g., Zaretskiy et al. 2010; Armanini et al. 2014), the Lattice Boltzmann (LB) methods (e.g., Shan,Chen 1993; Ma et al. 2010), the volume of fluid methods (e.g., López et al. 2000; Raeini et al. 2012) as well as the level-set methods (e.g., Prodanović,Bryant 2006). According to Fatt (1956), pore network modelling is designed to simulate fluid flow on a simplified structure described by a network of pore-bodies (nodes) connected by pore-throats (bonds), commonly referred to as a pore network model (PNM). Each network element (i.e. node or bond) is associated with a regular (e.g. a star, triangle, square, or circle) cross-section and assigned with a set of geometrical properties (e.g. radii, volume, shape factor, and length). Fluid dynamics (e.g. hydraulic conductance, capillary pressure) at each network element can be determined analytically for single-phase and multi-phase flow under specific assumptions (e.g. quasi-static flow), consequently pore network modelling is computationally more efficient than direct simulation method (Vogel and Roth 2001; Valvatne and Blunt 2004; Øren and Bakke 2002; Ryazanov et al. 2009; Jiang et al. 2007; 2013). Pore network modelling has been shown to be able to predict multi-phase properties, not only for homogeneous pore systems (e.g. sandstones) but also for heterogeneous multi-scale pore structures (e.g. carbonates), if the extracted pore networks describe the "true" topology and essential geometry of the pore space faithfully (Blunt et al. 2013).

The PNM is utilised to represent the pore space of rock models in a sense of topological equivalence, in general it can be constructed by maximal ball fitting (e.g., Silin and Patzek 2006; Dong,Blunt 2009) or medial axis (MA) separating (e.g., Lindquist and Venkatarangan 1999; Jiang et al. 2007). The former yields a PNM by identifying every local largest inscribed ball as a pore-body and every chain of smaller balls connecting two local largest balls as a pore-throat. The latter constructs a PNM through separating each MA into a set of junctions from which several line-segments spread out, and then partitioning the pore space into volumetric nodes and bonds corresponding to the separated local MA structure. It is obvious that the PNM by the MA-based method is strongly influenced by the MA extraction approaches, which can be categorised as either transforming or thinning algorithms. According to Thovert et al. (1993), the concept-based method focuses on searching all the pore voxels that are mostly far from solid phase, and the searching is often implemented by certain mathematical transformations. The resultant structure of a single voxel in thickness may have line-segments and surfaces, called medial axes and medial surfaces, respectively, in this work to differ them. This method cannot preserve pore connectivity and is computationally expensive. By contrast, the thinning algorithm retaining pore voxels after removing voxels as many as possible in the pore space produces MAs much faster and requires a small amount memory, and most importantly it yields a pore skeleton that has the desirable features: central locating and homotopic. The first feature of retaining voxels in pore centres can be ensured if the thinning process is controlled by a distance map, but the second one of preserving pore topology requires the application of many concepts in digital topology (Kong et al. 1992). For a complex pore system like the slit-like pores or fracture openings, the constructed skeleton must be a set of central lines that excludes any surfaces if only the concept of simple point is used in the thinning algorithm. To preserve on a pore skeleton the natural features of pores/voids in rock matrixes and in fractures, Jiang et al. (2017) introduces a thinning approach based on the concept of surface point so that the extracted skeleton contains not only MAs but also MSs. As far as the authors are aware, prior to the publication of Jiang et al. (2017), no thinning method has been reported in the literature for that geologically complex rocks like fractured carbonates, which are composed of two types of porous constituents: rock matrix and open (micro-)fractures that intersect with matrixes and/or themselves. Rock matrix contains cylinder/ball-like pores, which is disrupted by micro-fractures with slit-shaped opening voids. Jiang et al. (2017) developed an algorithm capable of

simultaneously extracting MAs from matrixes and MSs from fractures, which together define a "better" skeleton to capture the "true" morphology and topology of the pore-void space in fractured rocks. Such a skeleton captures the pore connectivity and geometry in matrixes through MAs and that in fractures through MS, and additionally the method tears off all skeleton fringes (see Fig. 1) that are close to fracture boundaries and connecting to rock matrixes. The skeleton fringes are considered redundant because fluids do not prefer to flow along fracture corners. Each MA is a group of connected pore voxels with a single connection at each MA voxel, except a junction voxel that allows multiple connections, while each MS is a set of connected voxels that form a central surface with multiple connections at each MS voxel. Jiang et al. (2017) developed a method that in effect discretises the pore skeleton into a PNM via further pulling apart of MSs into artificial MAs. The extracted PNM is optimal in many aspects: 1) capturing the full pore connectivity; 2) preserving the natural pore connectivity not only in matrixes and fractures but also in matrix-fracture regions; 3) sprawling a sub-network to form a flow path between each pair of the locations of local largest apertures; and 4) facilitating geometry properties to be measured locally and assigned to every network element. The network construction method is verified to be able to produce PNMs suitable for simulating single- and multi-phase flow of quasi-static drainage and imbibition processes at high accuracy.

In petrophysical analysis, estimating permeability and capillary pressure is usually the precursor for determining a comprehensive set of more complex properties, such as relative permeability. The objective of the work reported in this paper is to develop a much simpler and more efficient skeleton discretisation, a simpler PNM, and a simpler pore network simulator to meet the minimal requirements for estimating permeability and capillary pressure with upmost efficiency and acceptable accuracy. Unlike the discretisation method of Jiang et al. (2017), in this work we develop a new method that takes a radically different idea. Rather than sprawling a sub-network at selected voxels, we take every skeleton voxel into consideration by treating it as a virtual node, and connects each pair of skeleton voxels with a virtual link, that is, a bond, as long as they meet certain criteria consistent with the orientation of each MS. This idea can be directly applied to each MA. Consequentially, this leads to an in-place discretisation of pore skeletons that ensures the full topological representation of the pore-void space through MAs, MSs and the skeleton voxels in between. In order to estimate permeability and capillary pressure, we consider every MA link or each of its adjacent nodes as a cylinder and assign each with a radius and a length. However, we treat every MS link or each of its adjacent nodes as a cuboid and assign each with a radius, an aperture and a length. These quantities are locally measured at every skeleton voxel. For calculating hydraulic conductance and capillary pressure, we apply the Hagen-Poiseuille formula and the Yong-Laplace equation for every virtual link in both matrix pores and matrix-fracture interacting regions, and the cubic law, and a modified Yong-Laplace equation, for every virtual link in fractures, respectively. We do not apply the cubic law to the whole fracture, but locally (called "local cubic law" by Berkowitz 2002) to accommodate variable apertures, roughness and non-planar openings of fractures (Eker,Akin 2006).

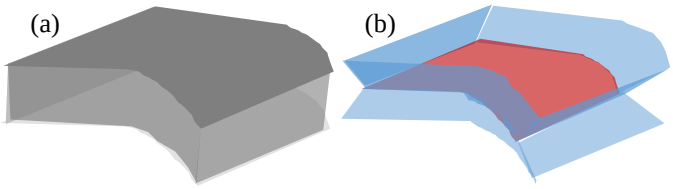

Fig. 1 A fracture (a) and its skeleton (b) composed of skeleton fringes (in blue) and central surfaces (in red). The central surfaces are referred to as the medial surfaces (MSs) in this work

In section 2 we describe in detail our methodology outlined above. In section 3 using several selected models, we verify our methods by comparing permeability and two fluid-phase distributions under

capillary-dominant drainage displacement simulated on respective virtual networks with those of single-phase Lattice Boltzmann simulations, and macroscopic fluid distributions obtained from a laboratory flooding experiment by Karpyn et al. (2007), respectively. Sensitivity studies are performed to further confirm that the proposed methods are accurate and computationally efficient. Section 4 gives conclusion from this work.

2. Methodology

In this work, a porous medium is treated as a pore-solid system by ignoring multiple mineral components in rocks, and takes a form of a 3D binary image (i.e. model), in which each voxel is either pore or solid and can be conventionally modelled by a cube.

In the cube voxel model, three neighbourhoods can be defined for a voxel p (see Fig. 2):

1) $N_6(p)$ – a set of neighbouring voxels that share a face with p;
2) $N_{18}(p)$ – a set of neighbouring voxels that share an edge with p;
3) $N_{26}(p)$ – a set of neighbouring voxels that share a vertex with p.

Obviously, the following holds: $N_6(p) \subset N_{18}(p) \subset N_{26}(p)$, but each voxel in $N_{18}(p)$ - $N_6(p)$ shares an edge only with p.

A voxel q is called an α-neighbour of p, namely q is α-adjacent to p, if $q \in N_\alpha(p)$, for $\alpha = 6$, 18 or 26. As stated by Kong et al. (1992), foreground (pore) and background (solid) voxels must have distinct but coupled adjacencies, such as 26-adjacency for foreground voxels and 6-adjacency for background voxels, which is used in this work.

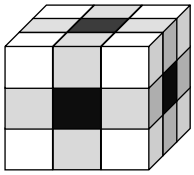

Fig. 2 three neighbourhoods of the central voxel: N_6 – 6 voxels in black, N_{18} – 18 voxels in black or grey, N_{26} – 26 voxels in black, grey or white

2.1 Discretisation of a pore skeleton with virtual links

As mentioned in Introduction, the pore skeleton extracted from a fractured rock using the algorithm of Jiang et al. (2017) might contain one or more medial axes (MAs) for ball-like pores in rock matrixes, and/or one or more medial surfaces (MSs) for fracture voids. Fig. 3(a) shows a fractured rock model created by embedding an artificial fracture (Fig. 3(b)) into a rock image; and Fig. 3(c, d) illustrate the distinct features between MS and MA with different colours. On such a skeleton each voxel is either on an MA or MS, called an MA or MS voxel. According to Jiang et al. (2017), an MS voxel can be precisely defined as a surface voxel of topological number $T_6 > 1$, and is retained if its removal would produce a hole/tunnel locally within its 26-neighourhood. Moreover, note that no skeleton fringes (see Fig. 1) are retained in the pore skeleton, so we can avoid redundant flow paths to be identified, which likely cause the overestimation of fluid mobility in PNM simulations.

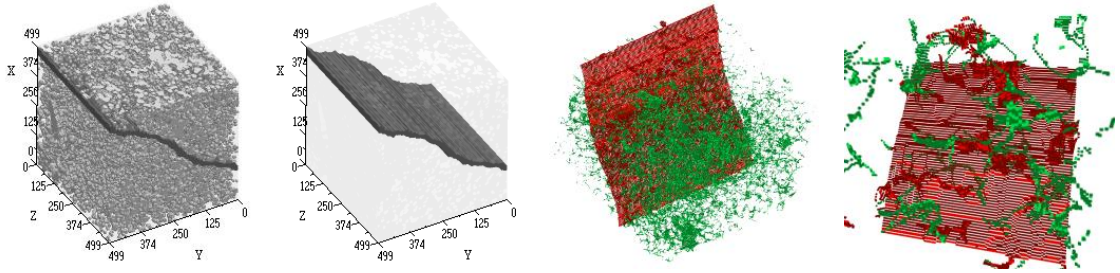

(a) (b) (c) (d)

Fig. 3 (a) a fractured model, (b) the embedded fracture, (c) the whole skeleton and (d) a zoomed-in view. Here, MA voxels are in green and MS voxels are in red

Given a pore skeleton, first we need to discretise it into a topological structure. Unlike the method of Jiang et al. (2017), we do not sprawl an optimal sub-network on each MS. Instead, we treat every skeleton voxel as a node and add a virtual link between two nodes, if they meet certain criteria defined below. The virtual likes are distinguished in the following, based on their locations of whether in matrixes or in fractures, aiming to capture pore connectivity correctly (see Fig. 4). In next section, we will show a case study of the 26-adjacency rather than the following one as the pore connectivity that result in overestimate of single-phase permeability.

1) MA links, each of which connects any two skeleton voxels that are 26-adjacent and at least one of them is an MA voxel, representing a possible flow path within matrix pores and/or matrix-fracture connections.
2) MS links, each of which connects any two MS voxels if (a) they share a face, called an *F*-link or (b) they share an edge only, called an *E*-link, and cannot be connected via consecutive 6-adjacent voxels.

The two exclusive criteria for MS links can be defined uniformly as follows and therefore can be determined more efficiently. For an MS voxel $p = (x_p, y_p, z_p)$, let $N_{MS}(p)$ be the set of all MS voxels that are 26-adjacent to p. We define the normal coordinate of p by a coordinate Ψ, i.e., x, y, or z, if each voxel in $N_{MS}(p)$ is most likely located on the Ψ-coordinate plane. Namely, we have:

$$\sum_{q\in N_{MS}(p)}|\Psi_p - \Psi_q| \le \sum_{q\in N_{MS}(p)}|\beta_p - \beta_q|, \text{ for } \beta = x, y, z \quad (1)$$

Fig. 4 shows a local configuration on a pore skeleton, composed of 9 MS and 8 MA voxels. According to the definition above, y is identified as the normal coordinate of voxel 5. Voxel 1 shares a face with 5, so the connection between them is valid; Voxel 5 shares an edge with 7 and their y-coordinates differ, thus their connection is valid too. There are many invalid connections too, such as the one between 5 and 2 and that between 5 and 8. Hence, we have precise definitions for MS links as follows:

For two MS voxels q and p with Ψ as the normal coordinate of p, (I) p is *F*-linked to q, if p shares a face with q, i.e. $q \in N_6(p)$; (II) p is *E*-linked to q, if (1) p shares an edge with q and (2) $|\Psi_p - \Psi_q| = 1$.

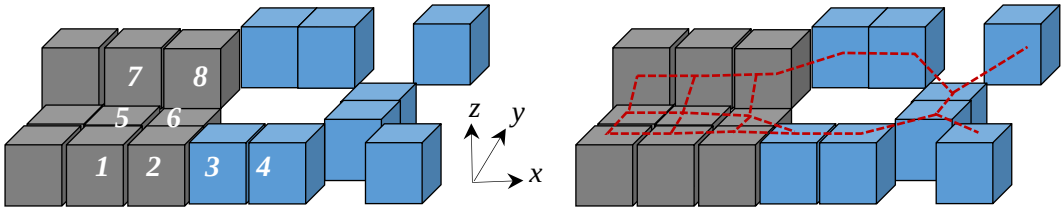

(a) (b)

Fig. 4 (a) a *F*-link between 5 and 1, a *E*-link between 5 and 7, and three MA links between 3 and 4, between 2 and 3, and between 3 and 6; (b) a topological structure (i.e. the red lines) formed by all valid virtual links. Here, MS voxels are in grey, and MA voxels in blue

2.2 Virtual network and estimating geometry properties

After creating all virtual links correctly, a topological pore structure is constructed (see Fig. 4(b)) as the framework of a virtual network, representing major flow paths on a pore skeleton. Next, a small number of geometrical properties are prescribed to each node or bond to accomplish the creation of a virtual network, so that single-phase flow and two-phase drainage processes can be performed on the resultant pore network. Inscribed radii and fracture apertures are measured at locations of the network elements and assigned to them, while the length of each link is calculated differently, described

below, due to the 2-dimensional nature of fractures that is distinct to matrix pores. Note that we do not compute a set of full geometry properties, as many of them are redundant for our simulations.

Link length

To simulate single-phase and two-phase drainage on a virtual network, we need to associate network elements with appropriate volumetric entities. For an MS link, as shown in Fig. 5(a, b), three tiny-fractures (i.e. cuboids) can be separated and associated with the two nodes and the MS link itself. The tiny-fracture for an MS link is actually the central region separated from the two tiny-fractures for the two adjacent nodes (see *P* and *Q* in Fig. 5(a, b) of apertures h_P and h_Q, respectively). The MS-link cuboid has the smaller aperture (i.e. h = min (h_P, h_Q) in Fig. 5(b)) as its height and a unit (i.e. w = 1) as its width. Regardless of the possibility of one node of an MA link being an MS voxel, we can uniformly associate MA links and the adjacent two nodes with three cylinders, which are the three parts separated from the cylinder between the two nodes, as shown in Fig. 5(c, d). The cylinder for a node has an inscribed radius, however the cylinder associated for an MA link has the harmonic mean of the two nodes' radii (see Fig. 5(d)). The length of a virtual link can be given by (see Fig. 5(b, d)):

$$L_{link} = \begin{cases} \tau, & for\ a\ MS\ link \\ \tau d, & for\ a\ MA\ link \end{cases}, \tag{2}$$

where τ ($0 < \tau < 1$) is a coefficient pre-defined, 1/3 is chosen in this work, which will be discussed later. The 'distance' between the two nodes (e.g., *P* and *Q* in Fig. 5(b)) adjacent to an MS link is defined by voxel length (i.e. d = 1 in Fig. 5(a)) due to the considered configuration shown in Fig. 5(b). Hence, the length of the central part (i.e. a tiny-fracture or a cylinder, see the pattern filled regions in Fig. 5(b, d)) is τ or τd for an MS or an MA link, respectively, as stated in Eq. (2), where d (see Fig. 5(d)) is the distance between the two nodes adjacent to an MS link.

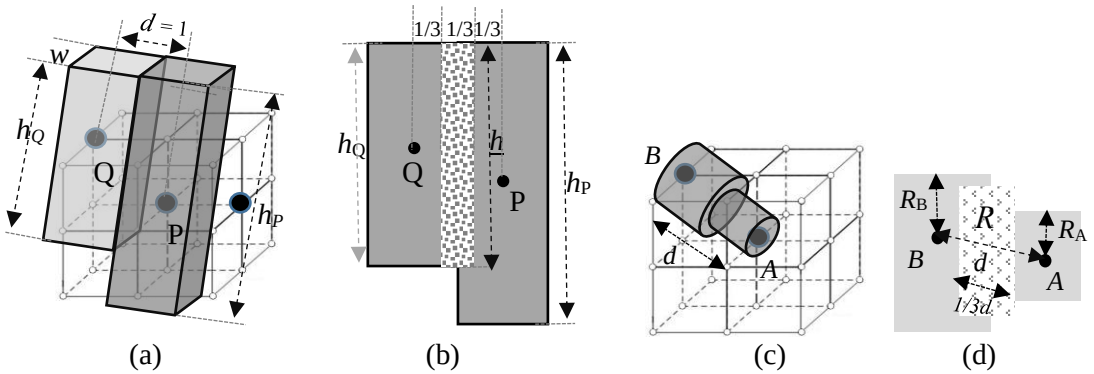

Fig. 5 Creation of virtual links: (a) two small fractures associated with two MS voxels *P* and *Q* adjacent to an *F*-link; (b) three tiny-fractures (cross-section view) separated from the two small fractures in (a); (c) two small cylinders associated with two nodes *A* and *B* adjacent to an MA link; (d) three cylinders (cross-section view) separated from the two small cylinders in (c)

Fracture aperture estimation

Inscribed radius is widely used to estimate fracture aperture. However, such a naive estimate, without considering the nature of a facture, i.e. variable apertures and rough walls, may become unreliable or not robust for fluid flow calculation. Here we implement an accurate approach to calculate fracture aperture.

A normal vector of a MS at a voxel, *M* (Fig. 6), can be determined by checking the voxel configuration in the 26- neighbourhood (i.e. $N_{MS}(M)$) at *M*. A covariance matrix is used to assemble all measured distances from *M* to its 26-adjacent MS voxels (Allgower,Schmidt 1985):

$$\mathrm{CV} = \sum_{p \in N_{MS}(\mathrm{M}))} (M - p) \otimes (M - p)\ , \tag{3}$$

where ⊗ denotes the outer product vector operator. We then calculate three eigenvalues ($\xi_1 > \xi_2 > \xi_3$) of CV using the Jacobi eigenvalue algorithm. Finally, the unit eigenvector corresponding to the smallest eigenvalue (ξ_3) is identified as the normal vector at *M* because the CV is a symmetric 3×3 positive semi-definite matrix. Furthermore, we can establish a normal vector field like the one shown in Fig. 6(b) to measure other properties such as the local apertures described below.

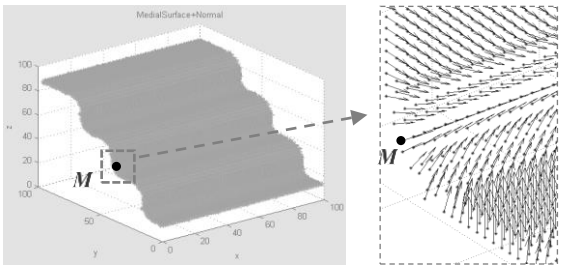

(a) (b)

Fig. 6 (a) An MS extracted from a stair-like fracture; (b) a zoomed-in normal vector field

From a voxel $p = (x_p, y_p, z_p)$, a ray-line can be given by:

$$\begin{cases} x = [x_p + \rho x_n] \\ y = [y_p + \rho y_n] \\ z = [z_p + \rho z_n] \end{cases}, \tag{4}$$

where (x_n, y_n, z_n) is the normal vector of an MS at p, [] is the operation to round a real value to the nearest integer, and $\rho > 0$ is the distance from (x, y, z) to p. Towards the two opposite directions, the ray-line intersects fracture walls with two points $p_1 = (x_1, y_1, z_1)$ and $p_2 = (x_2, y_2, z_2)$, and so a modified distance between p_1 and p_2 is defined as:

$$h^2(p) = d_x^2 + d_y^2 + d_z^2, \tag{5}$$

where $d_\alpha^2 = \begin{cases} 0, & \alpha_1 = \alpha_2 \\ (|\alpha_1 - \alpha_2| - 1)^2, & \alpha_1 \neq \alpha_2 \end{cases}$ for $\alpha = x, y, z$. In the work, we use h estimate the local fracture aperture.

2.3 Calculating conductance and permeability

For an MS link, the hydraulic conductance of each adjacent node or the link itself can be estimated by applying the cubic law (Witherspoon et al. 1980):

$$g = \frac{h^3 w}{12\mu}, \tag{6}$$

where w =1, μ is fluid viscosity, h is local fracture aperture.

It is desirable to treat MA links and the adjacent nodes differently, due to the different features of matrix pores in comparison to fracture openings. The cylinders associated a MS link or its adjacent nodes should be prescribed with inscribed radius R. Using the Hagen-Poiseuille equation (e.g., Patzek and Silin 2001), we compute the hydraulic conductance for a cylinder by:

$$g = \frac{cR^4}{\mu G}, \tag{7}$$

where c is a constant, which is ½ for circular cross-section with a fixed shape factor G = 0.079.

Typically, the effective conductance, g_{ij}, from node i to node j connected by a virtual link v is calculated by the harmonic mean (Oren et al. 1998):

$$\frac{L_{ij}}{g_{ij}} = \frac{L_i}{g_i} + \frac{L_j}{g_j} + \frac{L_v}{g_v}, \tag{8}$$

where g_v, g_i, and g_j are the three conductances for the link v and two adjacent nodes i and j, respectively. $L_i = L_j = L_v = 1/3$ if an MS link is involved; $L_i = L_j = L_v = 1/3d$ (see Eq. (2)) if an MA link is involved; and $L_{ij} = L_i + L_j + L_v$. Further, we have the flow rate from node i to node j:

$$q_{ij} = \frac{g_{ij}}{L_{ij}}\left(P_i - P_j\right), \tag{9}$$

where P_i and P_j are fluid pressures at node i and node j, respectively. Applying the law of mass conversation to every node i in a virtual network, we have:

$$\sum_j q_{ij} = 0, \tag{10}$$

where j is over all nodes that are connected to node i by a virtual link.

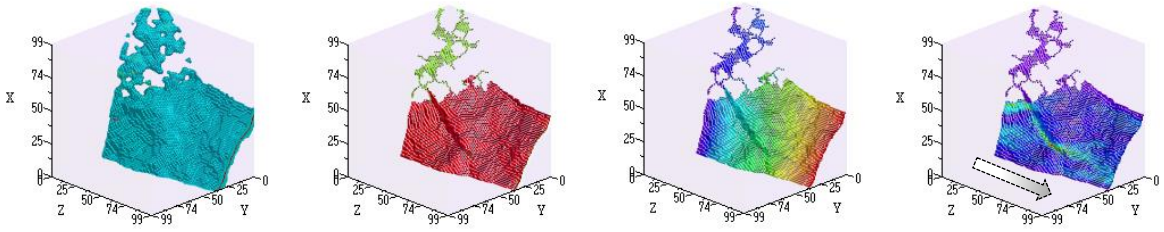

(a) (b) (c) (d)

Fig. 7 (a) a fracture-matrix pore system, (b) the extracted pore skeleton (MS in red, MA in green), (c) fluid pressure field on the skeleton, (d) flow rate field on the skeleton. The rainbow scheme is used in (c) and (d) to represent different pressures and flow rates, where the inlet is $z = 0$ and the outlet is $z = 99$

A fluid pressure field (Fig. 7(c)) on pore skeleton is further determined by solving a system of linear equations (i.e. Eq. (10)) over all nodes using the conjugate gradient algorithm (e.g., Oren et al. 1998). While a flow rate field (Fig. 7(d)) can be computed too using Eq. (9). Therefore, the total flow rate Q through the virtual network is obtained by summarising all flow rates of the virtual links that are directly connected to inlet (or outlet) boundary, and so the network permeability K can be estimated by applying the Darcy's law:

$$K = -\frac{Q\mu L}{A\nabla P}, \tag{11}$$

where L is the virtual network length from inlet to outlet in a coordinate direction, μ is fluid viscosity, ∇P is the pressure gradient (drop) between inlet and outlet, and A is the cross-sectional area of the corresponding rock sample.

2.4 Simulating drainage capillary pressure

The physical law that controls the displacements within pore systems for low capillary-number flows is the Yong-Laplace equation. The equation provides the relationship between the local capillary pressure, P_c, and the two principal radii (R_1 and R_2) of curvature of the interface between two phases by:

$$P_c = \gamma\left(\frac{1}{R_1} + \frac{1}{R_2}\right), \tag{12}$$

where γ is the interface tension. During the two-phase drainage displacement, the capillary (entry) pressure specifies a threshold for the invading non-wetting phase to displace the defending wetting phase within a pore or a local fracture opening – the displacement occurs locally if the pressure

difference (i.e. $P_{nw} - P_w$) between the two (i.e. wetting and non-wetting) phases is greater than P_c. The curvature of the two-phase interface can be directly related to the contact angle θ, which characterises wettability distribution within a pore of circular cross-section, with a radius R, thus we have the following Yong-Laplace equation for a cylinder:

$$P_c = \frac{2\gamma cos\theta}{R}. \tag{13}$$

Considering a fracture, R_1 in Eq. (12) corresponds to the curvature that is perpendicular to fracture walls, namely it is a local inscribed radius that can be used to estimate local aperture as mentioned above. R_2 is the radius of the in-place curvature, which counts for fluid local distribution (Hughes and Blunt 2001). So, R_2 can be assumed infinite in fractures, i.e. $1/R_2 = 0$, and thus for each MS voxel Eq. (12) can be modified more precisely as:

$$P_c = \frac{\gamma cos\theta}{h/2}, \tag{14}$$

where h is local fracture aperture. If we use the inscribed radius to estimate the aperture by $h \approx 2R$, the resultant P_c using Eq. (13) is approximately two times bigger than that of Eq. (14), which indicates that we certainly overestimate the capillary pressure within fractures using the original Laplace equation.

In our skeleton-based drainage simulation, a fractured rock sample is assumed initially saturated with wetting phase (WP), connected with a non-wetting phase (NWP) reservoir at the inlet and with a wetting phase (WP) reservoir at the outlet. Fig. 8 shows a fractured rock model with a resolution of 1μm per voxel, composed of five cylinders with inscribed radii of 3, 4, 6, 8, 12 voxels and three fracture apertures of 7, 9, and 13 voxels, the corresponding inscribed radii are 3, 4, and 6, respectively. The inlet plane is $x = 159$, on which variable NWP pressures P_{in} are put. The outlet plane is $x = 0$, on which a fixed pressure P_{out} is put through the whole simulating process. NWP first invades fracture at locations where its largest aperture is 13 voxels as the pressure drop ∇P, i.e. $P_{out} - P_{in}$, increases and exceeds a local P_c, determined by Eq. (14) rather than Eq. (13), even though the inscribed radius (6 voxels) is smaller than that of the largest pore. The process continues until NWP has invaded the whole pore-void space.

NWP displacing WP (i.e. drainage) without trapping is simulated as follows (see Fig. 8):

- Calculate inscribed radii for MA voxels and apertures for MS voxels, and set a sequence of pressure drops between the inlet and outlet planes, $\nabla P_1 < \nabla P_2 < \ldots$;
- Keep a constant pressure of WP on the outlet and increase the pressure of NWP on the inlet in an increment until a local P_c at one skeleton voxel is found such that $P_c < \nabla P$, the found voxel is marked as "invaded" in this loop. The NWP pressure continues increasing until all skeleton voxels that are connected to the inlet have been "invaded" one after another;
- In the end, all skeleton voxels are assigned sequence numbers to indicate the different invading steps. Based on the shortest distance criterion, the pore-void space is partitioned into different volumetric clusters, of which each has a unique sequence number. Note that a cluster looks like a cylinder or fracture if the corresponding sequence number comes from an MA or MS voxel, correspondingly;
- Determine a capillary pressure curve through correlating each pressure drop and the corresponding NWP volume.

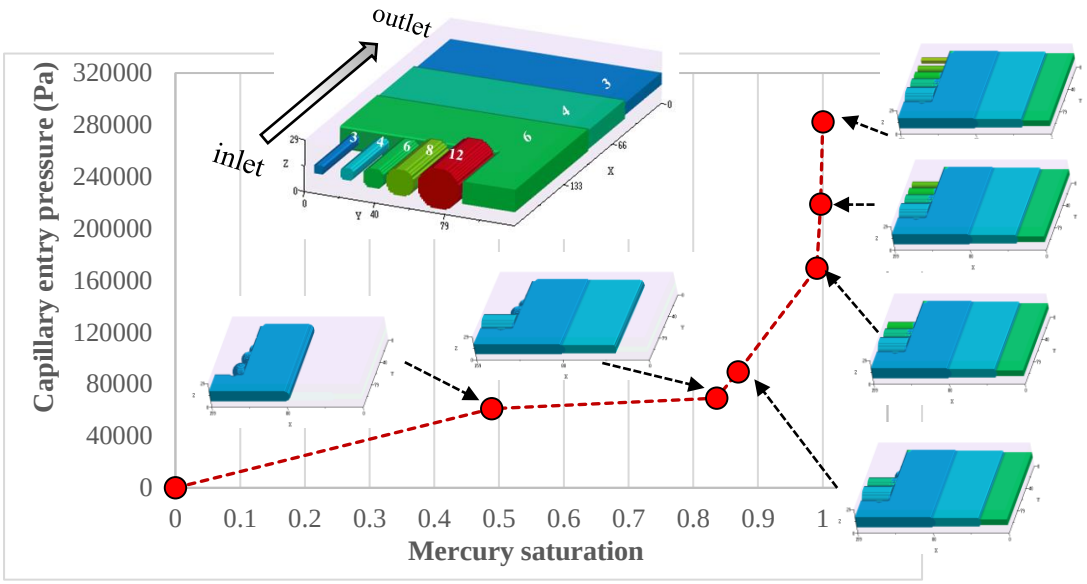

Fig. 8 A capillary pressure curve simulated for a model with 5 cylinders and 3 fractures. Here, the numbers (i.e. 3, 4, 6, 8, and 12) on the model denote inscribed radii

3. Results and discussions

In this section, models of fractured rocks have constructed to valid the skeleton-based (SB) method for simulating single-phase flow and two-phase drainage process.

3.1 Models and aperture estimations

Eight fractured models have been used to valid the SB method for permeability calculation. Table 1 lists all the models; among them, the first two models are synthetic while the remaining six are derived from X-ray CT images directly. We assume the voxel resolution of 1 μm/voxel for M_1 to M_6, and 12.8308 μm/voxel and 3.2 μm/voxel for M_7 and M_8, respectively. We estimate local fracture aperture at every MS voxel, and use the ratio of the mean aperture μ and standard aperture deviation σ, σ/μ, to approximately measure fracture roughness. The fracture apertures used in the calculation of μ and σ are obtained over a single fracture on a MS or multiple fractures on MSs in a model. The first two models have constant apertures of 9 and 5 voxels, respectively, and therefore are smooth. And the others have variable roughness with the roughest fractures in M_8.

models	M_1	M_2	M_3	M_4
pore-solid	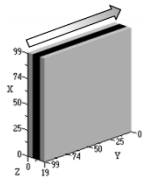	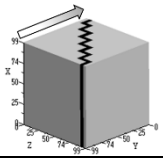	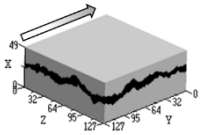	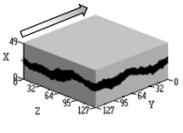
the pore space	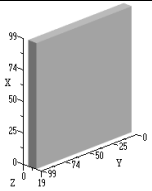	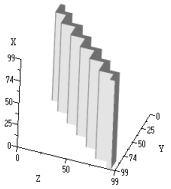	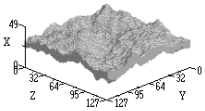	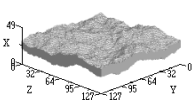
(μ, σ, σ/μ)	(9, 0, 0)	(5, 0, 0)	(7.23, 2.13, 0.295)	(10.75, 3.27,0.304)
models	M_5	M_6	M_7	M_8

pore-solid	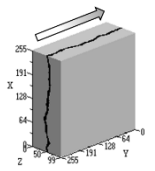	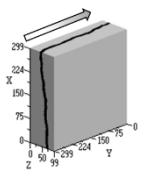	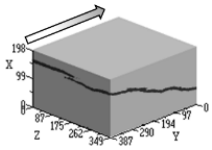	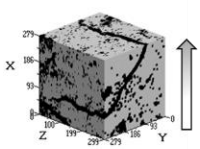
the pore space	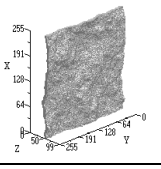	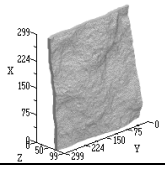	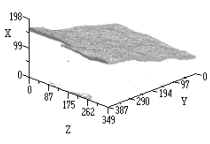	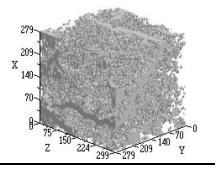
(μ, σ, σ/μ)	(6.24, 1.44, 0.231)	(9.92, 1.23, 0.124)	(123.84, 23.35, 0.189)	(26.94, 15.36, 0.57)

Table 1 Eight models of fractured rocks. μ (in μm) is mean aperture, and σ (in μm) is standard deviation of apertures; Arrows indicate the flow directions used in the simulations

Palabos (Paradis et al. 2016) is an open-source lattice Boltzmann (LB) package for CFD. We use the software to simulate single phase flow for the eight models listed in Table 1, and for each model LB permeability, K_{LB}, along the specified flow direction is determined to serve as a reference permeability for comparison with those to be calculated using the skeleton-based technique.

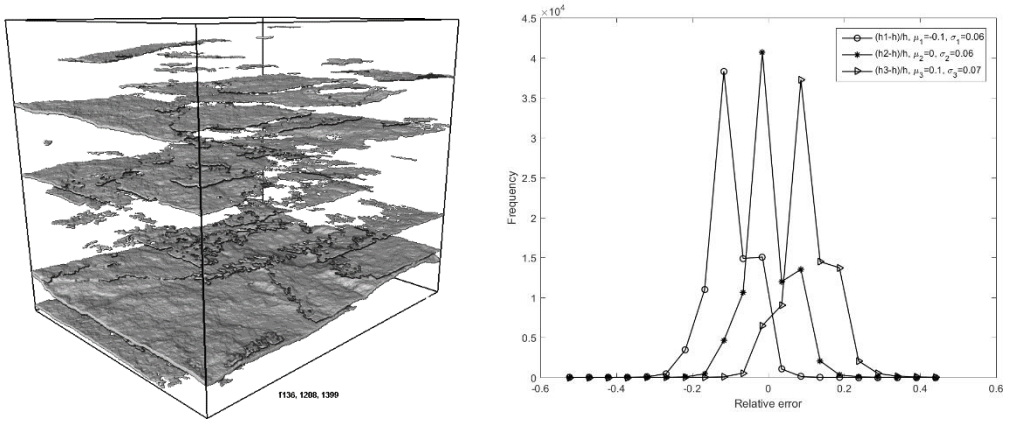

(a) (b)

Fig. 9 (a) an X-ray CT image with multiple fractures in 'parallel', (b) the three relative error frequencies for h_1, h_2, and h_3

As discussed previously, in addition to Eq. (5) the local aperture at each MS voxel can be estimated by $2R$, subjected to variability of one more or less voxel, denoted as $h_1 \approx 2R - 1$, $h_2 \approx 2R$ and $h_3 \approx 2R + 1$, where R is the inscribed radius at the MS voxel. Therefore, we calculate permeability for each model using our skeleton-based method on four virtual networks with the same topology but different local apertures, h, h_1, h_2 and h_3, denoted as $K_{SB,\zeta}$ where $\zeta = h$, h_1, h_2 or h_3, and compare the relative errors to K_{LB}, i.e. $(K_{SB,\zeta} - K_{LB})/K_{LB}$.

Fig. 9 illustrates the variability of h_1, h_2 and h_3 to h, i.e. $(h_1 - h)/h$, $(h_2 - h)/h$, and $(h_3 - h)/h$ over all fractures in a CT image (Fig. 9(a)) of a natural fractured rock. Note that its pore skeleton is composed of 98% MS and 2% of MA voxels. Fig. 9(b) shows the histograms of the relative errors, in which the averages and the standard deviations are -0.1, 0, and 0.1, and 0.06, 0.06, and 0.07, respectively. It is clear that the closest approximation to h is h_2.

3.2 Permeability calculation

For all models in Table 1, Table 2 presents the permeability estimates. Fig. 10 shows the relative errors of $(K_{SB,\zeta} - K_{LB})/K_{LB}$, for $\zeta = h$, h_1, h_2, and h_3.

models	M_1	M_2	M_3	M_4	M_5	M_6	M_7	M_8
K_{LB}(mD)	2977	70	469	1501	168.6	776.3	61,039	2304
$K_{SB,h}$(mD)	**2986**	**69.3**	**437.5**	**1633**	**171**	**773.3**	**65,231**	**2457**
$K_{SB,h1}$(mD)	2987	56.4	209	958	94.1	575	42811	2893
$K_{SB,h2}$(mD)	4097	98.6	358	1379	170	799	59868	3892
$K_{SB,h3}$(mD)	5453	157	549	1874	269	1064	79906	4940

Table 2 Permeabilities calculated by LB and the SB method for the eight models in Table 1 with four aperture estimations

From Fig. 10, it is clear that $K_{SB,h}$ matches closer to K_{LB} than any other $K_{SB,\zeta}$, $\zeta = h_1$, h_2, or h_3, with a maximum of relative error of only 9% and over 100%, respectively. This suggests that local aperture estimated by h is best suited for accurate permeability calculation. M_1 has an ideal fracture with an aperture of 9 μm, so the fracture permeability can be calculated by the cubic law as k = 6839.43 mD; Taking the sample porosity ($\varnothing$ = 0.441) into consideration, we then have the sample permeability $k\varnothing$ = 3016.19 mD. This analytical result matches that of the LB and our SB methods for the aperture estimation, h, but mismatches for h_2 or h_3. The distributions of the relative errors of $(K_{SB}\zeta - K_{LB})/K_{LB}$, $\zeta = h$, h_1, h_2 or h_3, are shown in Fig. 10 for the models in Table 1. The average relative deviations are -0.2314, -0.147, 0.614, and 0.019, for K_{SB} with apertures h_1, h_2, h_3, and h, respectively.

For the reference of computation efficiency of our SB method, we performed all simulations on a personal computer (Intel Xeon E5-2607V4(X2) CPU, 128G RAM), and recorded CPU time usages in seconds; the LB running times for the eight models are: 44, 3603, 39656, 32, 25207, 28832, 276657, and 97499, while the average running time of pore-network simulation for all models is 17.68. In contrast, our SB simulation for any model is far more efficient than the counterpart LB simulation.

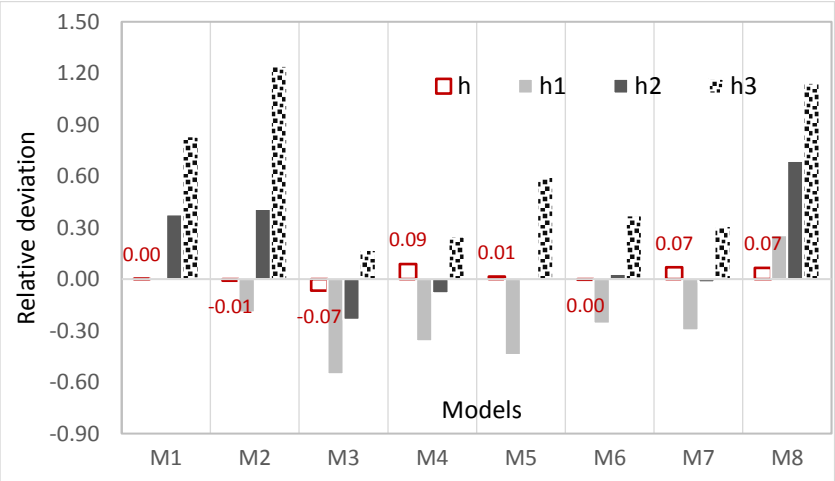

Fig. 10 Relative permeability deviations, $(K_{SB}\zeta - K_{LB})/K_{LB}$, calculated by our SB method with apertures $\zeta = h$, h_1, h_2, and h_3

3.3 Drainage simulation

We validate our method for simulating two-phase drainage process against the laboratory experiment results of Karpyn et al. (2007). Those authors have reported a multi-stage oil-water injection experiment, which was recorded by X-ray Micro-computed tomography (MCT) scans on a cylindrical sample (Fig. 11(a)) of Berea sandstone. An artificial fracture (Fig. 11(a)) was created using hydraulic press along the longitudinal axis. Prior to fluid injections, the sample is first dried and scanned to acquire a 3D CT image (Fig. 11(b)). The image is then utilised for detailed characterization of the fracture's inner structure, including aperture distribution, topography, roughness and contact regions (i.e. of zero aperture). After the dry sample (Fig. 11(a)) was saturated with tagged water (a viscosity of 1.2 cp and a density of 1.11 g/cm^3), a mixed oil (a viscosity of 5.0 cp and a density of 0.89 g/cm^3) was continuously injected into the sample from inlet end (i.e. the left edge in Fig. 11). The fracture aperture map (Fig. 11(c)) shows large apertures in light grey and white regions, smaller apertures in

dark grey regions, and zero apertures in black areas. The injection continued till irreducible water saturation was reached (around 0.35). The oil occupied the green regions while the water retained in the grey zones, as shown in Fig. 13. According to Karpyn et al. (2007), the sample has the strong wetting affinity of water, and the oil is non-wetting phase. Hence, the oil resides in larger open regions in the fracture while the water remains in small aperture zones.
We use the aperture map available to this work only to simulate the drainage process of the experiment to provide a validation of our method. We construct a fracture model (Fig. 11(d), 860×3116×31 voxels, 0.033 mm/voxel resolution, see Jiang et al. (2017) directly from the aperture map (Fig. 11(c)), assuming that the fracture is planar and symmetric about the fracture central plane. On this reconstructed fracture model, we extract its skeleton and construct a virtual pore network. Aperture probability distribution (i.e. the grey upside-down curve in Fig. 12) is then estimated to follow the lognormal distribution, with 98% of the surface voxels having apertures ranging from 33 μm up to 408 μm but ~900 μm at the largest, and 2% of the fracture plane area having a zero aperture.

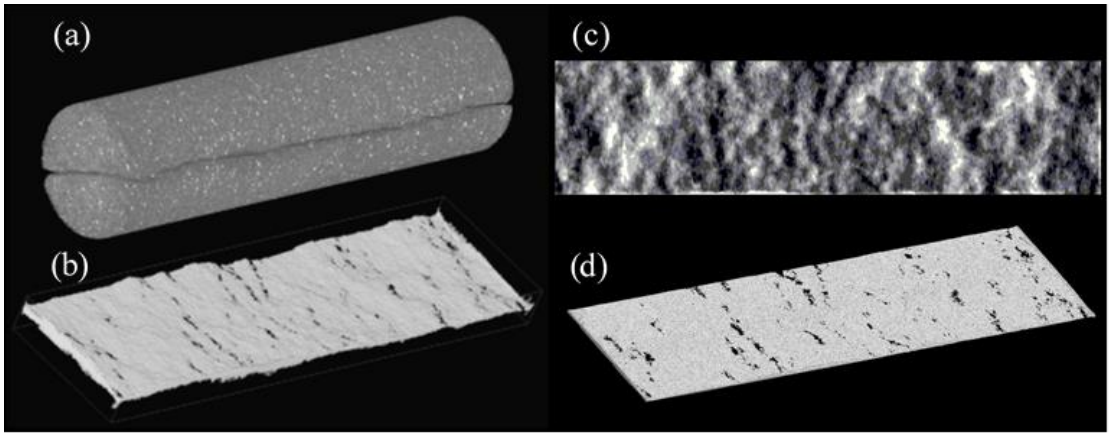

Fig. 11 View (Karpyn et al. 2007) of fractured Berea sandstone sample (a), the fracture resolved in a CT image (b), the aperture map (c), and a constructed fracture model from the aperture map (d)

To simulate the drainage process of the laboratory experiment as close as possible, we initialise our virtual network by filling it with water first. Then oil is injected into the model from its inlet on the left, while the water is allowed to be drained away from the same outlet on the right. We use the same fluid densities and viscosities of the experiment for fluids in our simulation. But for unknown values of the surface tension and contact angle, we apply 41 mN/m and 10^0 to the whole network.
We conduct a drainage simulation directly on the virtual network. The oil invasion starts at an entry pressure of 1822 Pa from the inlet plane (i.e. Y = 3115 in Fig. 12) and displaces more and more water within the fracture as the oil pressure increases gradually till a maximum oil pressure value of 6025 Pa is reached. Fig. 12 shows the capillary pressure and water saturation relationships of this simulation and the corresponding water situation variation in the pore network and therefore the fracture in space, when Pc is increased gradually. The rainbow colour scheme represents various invasion steps with the dark blue for the very earliest invasion, and the brown for the later invasion. Note that the flat part of the Pc curve in Fig. 12 is consistent with the single peak of the aperture distribution, indicating a large fraction of fracture voids with apertures within a narrow range.

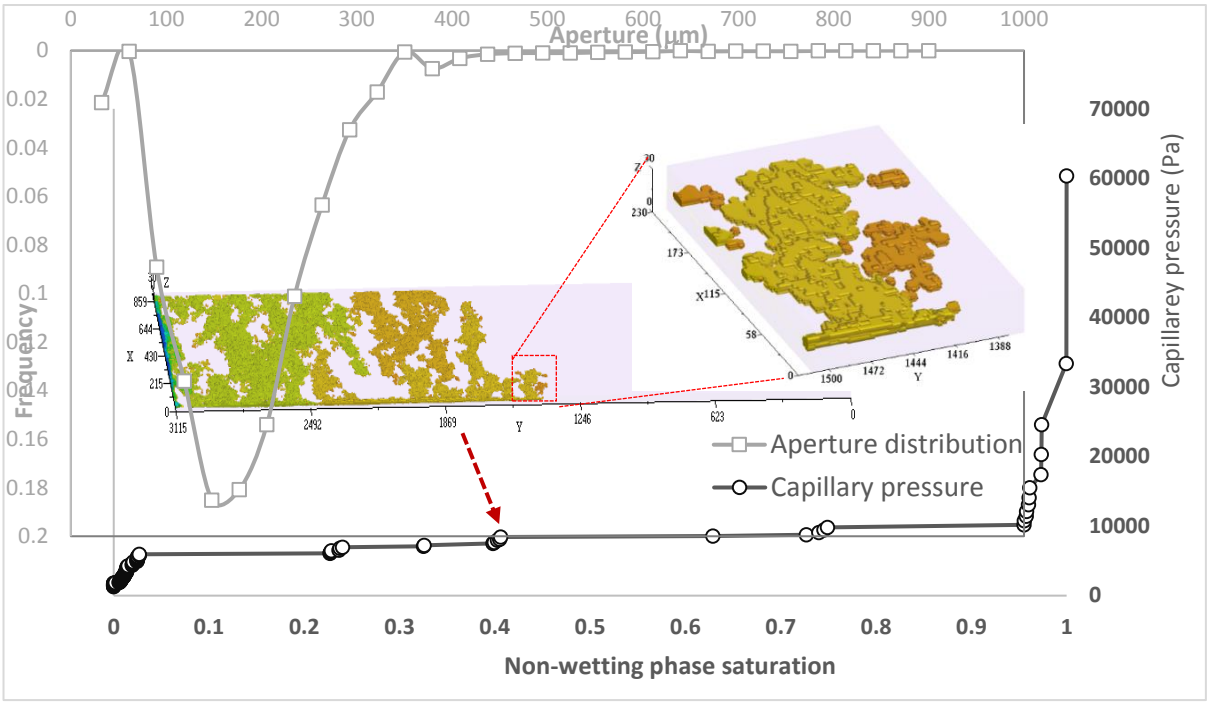

Fig. 12 Aperture distribution curve (in grey) and capillary pressure curve (in black)

.

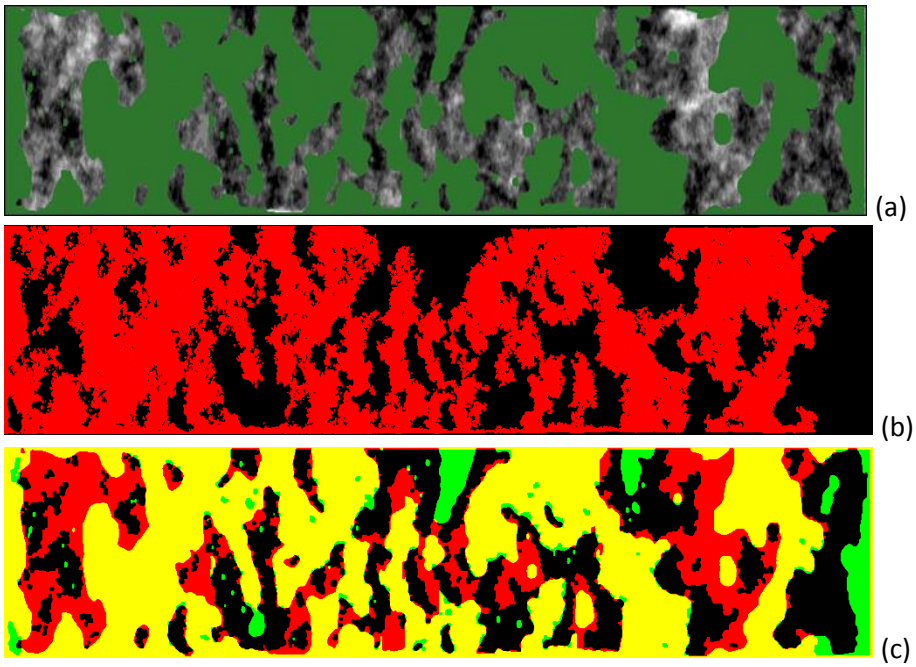

Fig. 13 Oil distributions: (a) oil globules (in green) under continuous oil injection, at irreducible water situation (0.35 stated but actually 0.47 counted by us) reported in Karpyn et al. (2007); (b) oil distributions (red area) simulated by our method with a water saturation of 0.339; (c) 89.6% oil-filled regions in the experimental case (green in (a)) that are overlapped by simulated oil-filled regions (red in (b)) in yellow

To compare experimental and simulated oil distributions, we terminate our simulation at an injection pressure at which the simulated water saturation is close to the experimental irreducible water situation of 0.35 (0.339 actually). Fig. 13(a, b) show the experimental and simulated oil distributions in green and red respectively, while Fig. 13(c) shows the overlapped oil distributions in yellow and the rest as in their respective colours as well as water-filled and locally close fracture apertures in

black. Note that over 89.6% of oil-filled area in the experimental case is also oil filled in simulated case. Thus, it suggests a good agreement between our simulation and the experiment although noticeable mismatches do exist. Of many possible reasons that may explain this discrepancy, three are more likely: (1) our simulation is not fully constrained to the experimental conditions, e.g. interfacial tension and contact angle; (2) the oil-filled green fraction in Fig. 13(a) that is copied from Karpyn et al. (2007) is actually measured voxel by voxel as around 0.53, which is significantly different from that of 0.65 stated in the paper; (3) our reconstructed fracture model (Fig. 11(d)) may not represent the true pore space accurately as the CT image (Fig. 11(b)) does, so that could result in a slightly different tortuosity to the flow paths within the fracture, especially for those near the sample boundaries.

3.4 26-adjacency on MS

From the discussion in Section 2.3, in a virtual network (see Fig. 3) two MS voxels are only considered connected in two situations, i.e. *F*-linked or *E*-linked. The 26-adjacency is used as a valid connection between two MA voxels or between one MA and one MS voxels, so it is important to investigate the impact of the 26-adjacency for MS voxels on single-phase flow. We re-compute all the permeabilities (denoted by K_{SBS}s) for the models in Table 1 under this connectivity condition, which allows any two MS voxels to be connected by a virtual link if the two voxels are 26-adjacent; and we compare the relative errors with the LB method again. The results are listed in Table 3.

models	M_1	M_2	M_3	M_4	M_5	M_6	M_7	M_8
K_{SB} (mD)	8008	182.32	1425.91	4878.61	489.88	2230.19	196,126	9097.14
$(K_{SB} - K_{LB})/K_{LB}$(%)	168.99	160.46	203.85	225.02	190.52	187.29	221.31	294.77

Table 3 Re-computed permeabilities and their relative errors for the eight models in **Table 1**

It is evident that considering any two 26-adjacent MS voxels connected in a virtual network could result in overestimation of permeability, because the actual fracture connectivity is wrongly magnified by ignoring the impossibility of fluid flow in diagonal and direct-edge-shared directions when each MS voxel is imagined as a tiny fracture. Namely, there should be no hydraulic conductance in the two situations: two MS voxels sharing a vertex or an edge but having alternative connections on the MS. This study highlights the importance of correctly defining the virtual link between MS voxels in our skeleton-based methods.

3.5 Sensitivity about link length

As mentioned in a previous section, an approapriate link length coefficient, $0 < \tau < 1$ (see Eq. (2)), needs to be chosen so that the actual length can be prescribed to all the MA/MS links in the virtual network. A sensitivity study has been carried out to determine such a value and found that $\tau = 1/3$ is an appropriate one, as summarised below.

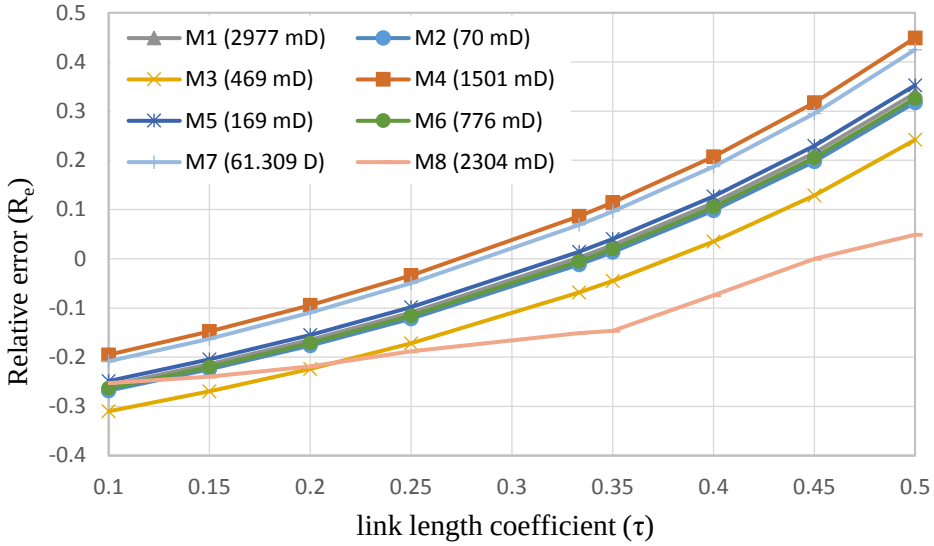

Fig. 14 Sensitivity of link length coefficient for the models in **Table 1**

For each model in Table 1, we re-caculate permeability K_{SB} and $(K_{SB} - K_{LB})/K_{LB}$ for every link length coefficient τ ranging from 0.1, 0.15, 0.2, 0.25, 1/3, 0.35, 0.4, 0.45, to 0.5 respectively, and then Fig. 14 shows the relative error for the different coeffecients.

4. Conclusions

In this paper, we have developed a new method for calculating permeability and capillary pressure of porous media samples directly from pore skeletons extracted using the algorithm of Jiang et al. (2017). Our main contributions in this work can be summarized as follows:

- Appropriately define the concept of virtual link and generate virtual network that captures not only the basic geometry but also the full topology of the pore-void space of fractured rocks;
- Implement an approach to calculate local apertures accurately in comparison to other inscribed radius-based approximations;
- Apply the cubic law not to a whole fracture but to its every local region between voxels on the medial surface, so as to achieve more accuracy and much higher efficiency;
- Develop an efficient method to simulate the drainage process directly on pore skeleton rather than the pore network with full geometrical properties, which is validated by comparing with Karpyn et al. (2007)'s experimental data;
- Conduct sensitivity studies to highlight many uncertainties and offer better choices, i.e. 1/3, F-/E-link, Eq.(5) for link length, connectivity and aperture estimation, respectively.

With the new skeleton-based methods established, in the future it is of interest to investigate how to represent the phase occupations at different 'locations' within nodes and virtual links on the pore skeleton to simulate multi-phase flow processes, in particular including imbibition process controlled by multiple displacement mechanisms, such as snap-off.

Note that it is difficult to validate Eq. (6) theoretically or numerically. With the proposed method of Eq. (5) to measure apertures, in this work Eq. (6) is demonstrated by various simulations to approximately represent the flow behaviours in the three-dimensional pore space, consequently it is a reasonable estimate of the conductance for each MS link. However, it is necessary to conduct further investigation of both the applicability of the cubic law and the estimation of the effective transport coefficients as functions of the intrinsic fracture geometrical characteristics.

Acknowledgements

This work is financially supported by National Natural Science Foundation of China (Grant No. 61572007) and theoretical research project of Sichuan (2014JY0105).

References

Allgower, E.L., Schmidt, P.H.: An algorithm for piecewise-linear approximation of an implicitly defined manifold. SIAM journal on numerical analysis **22**(2), 322-346 (1985)

Andrew, M., Bijeljic, B., Blunt, M.J.: Pore-scale imaging of trapped supercritical carbon dioxide in sandstones and carbonates. International Journal of Greenhouse Gas Control **22**, 1-14 (2014)

Armanini, A., Larcher, M., Nucci, E., Dumbser, M.: Submerged granular channel flows driven by gravity. Advances in water resources **63**, 1-10 (2014)

Arns, C.H., Bauget, F., Limaye, A., Sakellariou, A., Senden, T., Sheppard, A., Sok, R.M., Pinczewski, V., Bakke, S., Berge, L.I.: Pore scale characterization of carbonates using X-ray microtomography. Spe Journal **10**(04), 475-484 (2005)

Berkowitz, B.: Characterizing flow and transport in fractured geological media: A review. Advances in water resources **25**(8-12), 861-884 (2002)

Blunt, M.J., Bijeljic, B., Dong, H., Gharbi, O., Iglauer, S., Mostaghimi, P., Paluszny, A., Pentland, C.: Pore-scale imaging and modelling. Advances in Water Resources **51**, 197-216 (2013)

Dong, H., Blunt, M.J.: Pore-network extraction from micro-computerized-tomography images. Physical review E **80**(3), 036307 (2009)

Eker, E., Akin, S.: Lattice Boltzmann simulation of fluid flow in synthetic fractures. Transport in porous media **65**(3), 363-384 (2006)

Fatt, I.: The network model of porous media. (1956)

Geiger, S., Emmanuel, S.: Non‐Fourier thermal transport in fractured geological media. Water Resources Research **46**(7) (2010)

Huang, T., Jiang, Z., Van Dijke, M. I. J., Geiger, S., Petrovskyy, D.: Pore architecture reconstruction (PAR) of heterogeneous structure from 2D images. In: ENERGI Simulation Chair programme meeting, November, Heriot Watt University, UK. (2017)

Hughes, R.G., Blunt, M.J.: Network modeling of multiphase flow in fractures. Advances in Water Resources **24**(3-4), 409-421 (2001)

Jiang, Z., Dijke, M., Sorbie, K., Couples, G.: Representation of multiscale heterogeneity via multiscale pore networks. Water resources research **49**(9), 5437-5449 (2013)

Jiang, Z., van Dijke, M., Geiger, S., Ma, J., Couples, G., Li, X.: Pore network extraction for fractured porous media. Advances in Water Resources **107**, 280-289 (2017)

Jiang, Z., Wu, K., Couples, G., Van Dijke, M., Sorbie, K., Ma, J.: Efficient extraction of networks from three‐dimensional porous media. Water Resources Research **43**(12) (2007)

Karpyn, Z., Grader, A., Halleck, P.: Visualization of fluid occupancy in a rough fracture using micro-tomography. Journal of colloid and interface science **307**(1), 181-187 (2007)

Kong, T.Y., Roscoe, A.W., Rosenfeld, A.: Concepts of digital topology. Topology and its Applications **46**(3), 219-262 (1992)

López, A.M., Lloret, D., Serrat, J., Villanueva, J.J.: Multilocal creaseness based on the level-set extrinsic curvature. Computer Vision and Image Understanding **77**(2), 111-144 (2000)

Lindquist, W., Venkatarangan, A.: Investigating 3D geometry of porous media from high resolution images. Physics and Chemistry of the Earth, Part A: Solid Earth and Geodesy **24**(7), 593-599 (1999)

Ma, J., Wu, K., Jiang, Z., Couples, G.D.: SHIFT: An implementation for lattice Boltzmann simulation in low-porosity porous media. Physical Review E **81**(5), 056702 (2010)

Øren, P.-E., Bakke, S.: Process based reconstruction of sandstones and prediction of transportproperties. Transport in porous media **46**(2-3), 311-343 (2002)

Oren, P.-E., Bakke, S., Arntzen, O.J.: Extending predictive capabilities to network models. SPE journal **3**(04), 324-336 (1998)

Paradis, H., Andersson, M., Sundén, B.: Modeling of mass and charge transport in a solid oxide fuel cell anode structure by a 3D lattice Boltzmann approach. Heat and Mass Transfer **52**(8), 1529-1540 (2016)

Patzek, T., Silin, D.: Shape factor and hydraulic conductance in noncircular capillaries: I. One-phase creeping flow. Journal of colloid and interface science **236**(2), 295-304 (2001)

Prodanović, M., Bryant, S.L.: A level set method for determining critical curvatures for drainage and imbibition. Journal of colloid and interface science **304**(2), 442-458 (2006)

Raeini, A.Q., Blunt, M.J., Bijeljic, B.: Modelling two-phase flow in porous media at the pore scale using the volume-of-fluid method. Journal of Computational Physics **231**(17), 5653-5668 (2012)

Richardson, J., Kerver, J., Hafford, J., Osoba, J.: Laboratory determination of relative permeability. Journal of Petroleum Technology **4**(08), 187-196 (1952)

Rose, W., Bruce, W.: Evaluation of capillary character in petroleum reservoir rock. Journal of Petroleum Technology **1**(05), 127-142 (1949)

Ryazanov, A., Van Dijke, M., Sorbie, K.: Two-phase pore-network modelling: existence of oil layers during water invasion. Transport in Porous Media **80**(1), 79-99 (2009)

Shan, X., Chen, H.: Lattice Boltzmann model for simulating flows with multiple phases and components. Physical Review E **47**(3), 1815 (1993)

Silin, D., Patzek, T.: Pore space morphology analysis using maximal inscribed spheres. Physica A: Statistical mechanics and its applications **371**(2), 336-360 (2006)

Thovert, J., Salles, J., Adler, P.: Computerized characterization of the geometry of real porous media: their discretization, analysis and interpretation. Journal of microscopy **170**(1), 65-79 (1993)

Valvatne, P.H., Blunt, M.J.: Predictive pore‐scale modeling of two‐phase flow in mixed wet media. Water Resources Research **40**(7) (2004)

Vogel, H.-J., Roth, K.: Quantitative morphology and network representation of soil pore structure. Advances in water resources **24**(3-4), 233-242 (2001)

Wildenschild, D., Sheppard, A.P.: X-ray imaging and analysis techniques for quantifying pore-scale structure and processes in subsurface porous medium systems. Advances in Water Resources **51**, 217-246 (2013)

Witherspoon, P.A., Wang, J.S., Iwai, K., Gale, J.E.: Validity of cubic law for fluid flow in a deformable rock fracture. Water resources research **16**(6), 1016-1024 (1980)

Wu, K., Van Dijke, M.I., Couples, G.D., Jiang, Z., Ma, J., Sorbie, K.S., Crawford, J., Young, I., Zhang, X.: 3D stochastic modelling of heterogeneous porous media–applications to reservoir rocks. Transport in Porous Media **65**(3), 443-467 (2006)

Zaretskiy, Y., Geiger, S., Sorbie, K., Förster, M.: Efficient flow and transport simulations in reconstructed 3D pore geometries. Advances in Water Resources **33**(12), 1508-1516 (2010)